Multivariable Analysis and Control of a VSC Back-to-Back Converter Interfacing Two ac Systems

Igor D. N. de Souza, Pedro M. de Almeida, Gabriel A. Fogli, Pedro G. Barbosa

***Abstract*—This work analyses a voltage source back-to-back converter interfacing two alternating current systems from a multivariable perspective. Since the plant is not functionally controllable, frequency-dependent relative gain array analysis is carried out to aid in the choice of the most suitable variables to be controlled in a specific frequency range. This analysis is crucial to choose the low- and high-frequency controllers. A systematic approach is developed to tune a centralized optimal control. Validation of theoretical analysis and proposed multiple-input multiple-output (MIMO) control law is performed through experimental results.**

***Keywords*—Back-to-back converter, multivariable optimal control, frequency-dependent relative gain array.**

I. Introduction

MANY solutions proposed to improve the electrical system steady-state and dynamic characteristics are power electronic converters based. They are designed to make the system more reliable, efficient and robust. Among them, the back-to-back (BTB) topology is largely employed as an efficient interface between two subsystems [1].

According to [1], the reasons of the widespread employment of BTB topology are twofold: (*i*) wide control of bidirectional energy flow; and (*ii*) control of the active power in addition to independent control of reactive power, allowing flexible operation. The previous features lead to the interesting property of fast energy flow regulation, which in turn provide the balance between two different ac systems [2]. Thanks to these advantageous characteristics, the back-to-back voltage source converter (BTB-VSC) is broadly used in the industrial sector [3].

The classical control law applied to BTB converters is based on cascaded inner ac current and external dc-link voltage controllers [4, 5]. The main reason for the popularity of this approach is the fact that it is possible to decouple the inner and outer outer controller tuning. Furthermore, the control loops can be treated as single-input-single-output (SISO) systems and, therefore, allowing the use of well-known classical approaches to design the compensators [6]. The downside of this approach is not taking into account the intrinsic multivariable characteristic of the plant.

On one hand, decentralized techniques attempt to control multivariable plants by a suitable decomposition into SISO control loops. It has the advantage of easy implementation and controller's gains tuning. On the other hand, centralized approaches usually result in better performance at the cost of higher complexity [7]. Jovcic et al. [8] have shown that classical proportional-integral (PI) controllers' approach is not able to ensure axes decoupling under parametric variations. Control laws based on the minimization of quadratic cost functions have also been applied to voltage source converters (VSC) in order to optimize the SISO control systems, as well as to ensure robustness [9, 10]. MIMO and MIMO/linear quadratic regulator (LQR) controllers are used in [11, 12] and [13], respectively, to improve the performance in comparison with SISO axis decoupling control. A MIMO/LQR capable of damping the output filter's resonance and while reducing axis cross coupling is shown [14]. The unified MIMO control approach developed by Rodriguez-Cabero et al. [15] ensures a better performance over classical strategies for converters with third-order inductive-capacitive-inductive (LCL) filters. In [2] the proposed state-space control provides dc-bus and active and reactive powers fast regulation. Variations in the filter parameters, dc capacitance, grid inductance, and grid voltage levels are employed to evaluate robustness levels.

This paper attempts to fill some gaps in the analysis and control of BTB using MIMO tools. As a consequence, the following points are regarded as the main contribution to the field: 1) Analyze the BTB from a MIMO perspective; 2) Choose the most suitable variables that can be directly regulated according to the frequency-dependent relative gain array analysis; 3) Calculate the optimal feedback gains via LQR technique; 4) Use suitable sensitivity transfer function to assist in the weighting procedure; 5) making the tuning systematic; 6) Validate the analysis and design through experimental results.

II. BTB Converter Description and Modeling

The system under study is depicted in Fig. 1. It consists of two VSCs that are connected to their respective three-phase secondary networks through a first-order low-pass filter. Besides, both VSC shares the same dc link, featuring a *back-to-back* system.

By applying the kirchhoff's laws the the system depicted in Fig. 1, and afterwards linearizing it around an equilibrium point yields

$$\dot{\boldsymbol{x}} = \boldsymbol{\mathcal{A}}\boldsymbol{x} + \boldsymbol{\mathcal{B}}\boldsymbol{u} + \boldsymbol{\mathcal{B}}_w\boldsymbol{w} \tag{1}$$

This research was supported in part by Coordenação de Aperfeiçoamento de Pessoal de Nível Superior (CAPES) under Grant 001, Conselho Nacional de Desenvolvimento Científico e Tecnológico (CNPq) under grant 302364/2022-6 and 404068/2020-0, Fundação de Amparo à Pesquisa do Estado de Minas Gerais (FAPEMIG) under grant APQ-03609-17 and Instituto Nacional de Energia Elétrica (INERGE).

Igor D. N. Souza is with Universidade Federal de Ouro Preto, Brazil. Pedro M. Almeida and Pedro G. Barbosa are with Universidade Federal de Juiz de Fora, Brazil, (e-mail: pedro.machado@ufjf.edu.br). Gabriel A. Fogli is with Universidade Federal de Minas Gerais.

Paper submitted to the International Conference on Power Systems Transients (IPST2023) in Thessaloniki, Greece, June 12-15, 2023.

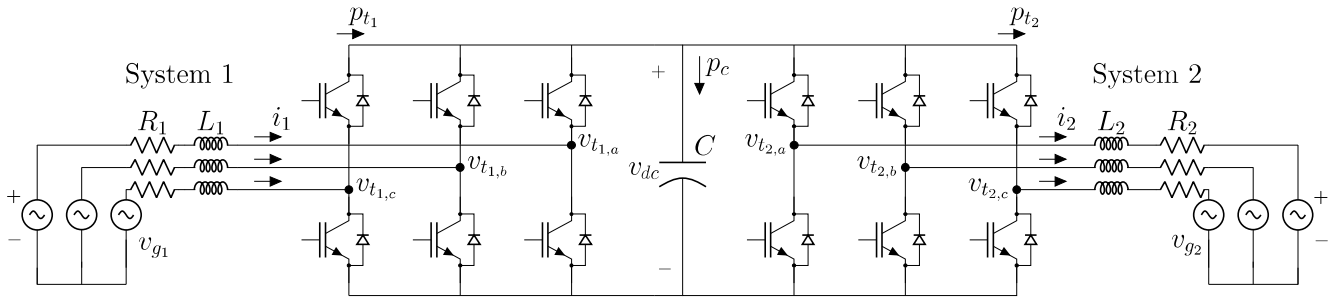

Fig. 1. Schematic diagram of BTB connection to AC grid 1 and 2.

where,

$$\boldsymbol{\mathcal{A}} = \begin{bmatrix} -\frac{R_1}{L_1} & \omega_1 & 0 & 0 & -\frac{M_{1,d}}{\sqrt{3}L_1} \\ -\omega_1 & -\frac{R_1}{L_1} & 0 & 0 & -\frac{M_{1,q}}{\sqrt{3}L_1} \\ 0 & 0 & -\frac{R_2}{L_2} & \omega_2 & +\frac{M_{2,d}}{\sqrt{3}L_2} \\ 0 & 0 & -\omega_2 & -\frac{R_2}{L_2} & +\frac{M_{2,q}}{\sqrt{3}L_2} \\ \frac{\sqrt{3}M_{1,d}}{2C} & \frac{\sqrt{3}M_{1,q}}{2C} & -\frac{\sqrt{3}M_{2,d}}{2C} & -\frac{\sqrt{3}M_{2,q}}{2C} & 0 \end{bmatrix}$$

$$\boldsymbol{\mathcal{B}} = \begin{bmatrix} -\frac{V_{dc}}{\sqrt{3}L_1} & 0 & 0 & 0 \\ 0 & -\frac{V_{dc}}{\sqrt{3}L_1} & 0 & 0 \\ 0 & 0 & \frac{V_{dc}}{\sqrt{3}L_2} & 0 \\ 0 & 0 & 0 & \frac{V_{dc}}{\sqrt{3}L_2} \\ \frac{\sqrt{3}I_{1,d}}{2C} & \frac{\sqrt{3}I_{1,q}}{2C} & -\frac{\sqrt{3}I_{2,d}}{2C} & -\frac{\sqrt{3}I_{2,q}}{2C} \end{bmatrix}$$

$$\boldsymbol{\mathcal{B}}_w = \begin{bmatrix} \frac{1}{L_1} & 0 & 0 & 0 \\ 0 & \frac{1}{L_1} & 0 & 0 \\ 0 & 0 & -\frac{1}{L_2} & 0 \\ 0 & 0 & 0 & -\frac{1}{L_2} \\ 0 & 0 & 0 & 0 \end{bmatrix}$$

$$\boldsymbol{x} = \begin{bmatrix} \tilde{i}_{1,d} \\ \tilde{i}_{1,q} \\ \tilde{i}_{2,d} \\ \tilde{i}_{2,q} \\ \tilde{v}_{dc} \end{bmatrix}, \boldsymbol{u} = \begin{bmatrix} \tilde{m}_{1,d} \\ \tilde{m}_{1,q} \\ \tilde{m}_{2,d} \\ \tilde{m}_{2,q} \end{bmatrix}, \boldsymbol{w} = \begin{bmatrix} \tilde{v}_{g_{1,d}} \\ \tilde{v}_{g_{1,q}} \\ \tilde{v}_{g_{2,d}} \\ \tilde{v}_{g_{2,q}} \end{bmatrix} \tag{2}$$

$\boldsymbol{x}$ is the state vector, $\boldsymbol{u}$ is the input vector, $\boldsymbol{w}$ is the disturbance vector. v_{dc} is voltage across the dc-bus; $i_{1,d}$, $i_{1,q}$, $i_{2,d}$ and $i_{2,q}$ are converter's output currents; $v_{g_{1,d}}$, $v_{g_{1,q}}$, $v_{g_{2,d}}$, $v_{g_{2,q}}$ are the mains voltage; $m_{1,d}$, $m_{1,q}$, $m_{2,d}$ and $m_{2,q}$ are the control signals; L_1, L_2, R_1 and R_2 are the interface filter's inductances and its intrinsic resistances, respectively. ω_1 and ω_2 are the frequencies. The subscripts 1 and 2, respectively, are used to identify subsystem 1 and 2. Moreover, the notation $\tilde{v}_{dc}$ represents small perturbations around the operating point V_{dc}. Thus, the state variable is represented by $v_{dc} = V_{dc} + \tilde{v}_{dc}$. A Double Second-order Generalized Integrator Phase-Locked-Loop (DSOGI-PLL) is used to track both grid's frequency and angle to perform the $abc/dq0$ coordinate transformation [16].

III. BTB Converter Analysis as a Multivariable System

A dynamical system is called multivariable if more than one variable is directly controlled. Some phenomena occur exclusively in systems of this type, and there is no correspondence in SISO systems. As an example, one of the most important differences between a SISO scalar system and a MIMO system is the presence of directions. This fact is crucial in the analysis of non-square plants, like the BTB. For the case where there are less inputs than outputs, there exists output directions that cannot be arbitrarily controlled [7, 17]. This property is called functional controllability [17]. For the plant under analysis there is one output direction which cannot be arbitrarily controlled [18]. This will be carried out by using the frequency-dependent relative gain array (RGA) [19].

A. Frequency-dependent RGA analysis

Chang and Yu [20] recognized that the row sums of the RGA stayed between zero and one for non-square plants with full column rank (more outputs than inputs) [21]. While Cao [22] have shown that this number can be used to identify whether the corresponding output is easy, hard or even impossible to control. If the sum is close to unity, the easier it is to control. Conversely, the closer to zero, the more difficult is to regulate this variable. As a consequence, this tool is suitable to help in the decision of the controlled variables as a function of the frequency. The RGA is defined as:

$$\Lambda(\mathbf{G}(j\omega)) = \mathbf{G}(j\omega) \odot (\mathbf{G}^{-1}(j\omega))^{\dagger}, \tag{3}$$

where, $\odot$ denotes element-wise multiplication and $\dagger$ the pseudoinverse.

The frequency-dependent RGA row sums are illustrated in Fig. 2. The system's parameters are given in Fig. I.

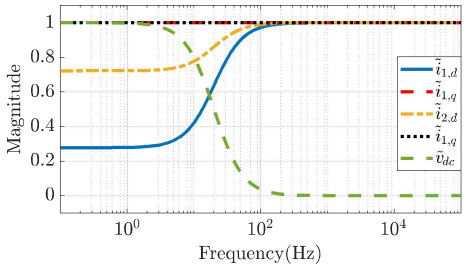

Fig. 2. Row sums of $\Lambda(\boldsymbol{\mathcal{G}}(j\omega))$.

According to Fig.2, $\tilde{i}_{1,q}$ and $\tilde{i}_{2,q}$, as their sum is 1 for all frequencies, they can be arbitrarily controlled at any frequency spectrum. This fact makes completely sense since the reactive power at each side is independent from the other. Conversely,

TABLE I
BTB PARAMETERS.

System Parameters	
Description	Value
Grid 1 and 2 fundamental frequency (f_1,f_2)	60 Hz
Switching frequency (f_{sw})	20 kHz
Sampling frequency (f_S)	20 kHz
Grid 1 voltage d-axis ($V_{g_{1,d}}$)	180 V
Grid 1 voltage q-axis ($V_{g_{1,q}}$)	0 V
Grid 2 voltage d-axis ($V_{g_{2,d}}$)	90 V
Grid 2 voltage q-axis ($V_{g_{2,q}}$)	0 V
DC-link voltage (V_{dc})	400 V
BTB inductances (L_1,L_2)	1 mH
BTB resistances (R_1, R_2)	0.3 Ω
DC-link capacitance (C)	6 mF
Operation points	
Description	Valor
Input current d-axis ($I_{1,d}$)	15 A
Input current q-axis ($I_{1,q}$)	0 A
Output current d-axis ($I_{2,d}$)	26.8 A
Output current q-axis ($I_{2,q}$)	0 A
Modulation index d-axis of GIC 1 ($M_{1,d}$)	0.7599
Modulation index q-axis of GIC 1 ($M_{1,q}$)	-0.0244
Modulation index d-axis of GIC 2 ($M_{2,d}$)	0.4245
Modulation index q-axis of GIC 2 ($M_{2,q}$)	0.0438

$\tilde{v}_{dc}$ can only be easily controlled at low frequencies. It is impossible to control it at higher frequencies since the value is almost zero. Besides the previous variables, there is room for another variable to be controlled at low frequency, since there are four inputs. In this sense, between the remaining variables, $\tilde{i}_{2,d}$ should be chosen, since the sum of the row elements of $\Lambda(\boldsymbol{\mathcal{G}}(j\omega))$ regarding this variable is closer to unity than $\tilde{i}_{1,d}$.

Contrastingly, notice that at high frequencies the dc-capacitor voltage cannot be controlled and all four currents can be easily arbitrarily controlled. This fact can be explained by the fact that the current harmonics do not generate average active power as the voltages are sinusoidal. Therefore, at high frequency the current control of both sides is decoupled and can be used to compensate harmonics components. Moreover, as there is no, in higher frequencies, average active power flow in the BTB dc-side, it is not possible to control $\tilde{v}_{dc}$, as stated before. Notice that at around 10 Hz the $\tilde{v}_{dc}$ and $\tilde{i}_{1,d}$ relative curves intersect each order at the magnitude of 0.6. This means that, as the frequency increase above 10 Hz, the bus-voltage control becomes more and more difficult, demanding more and more energy to perform this task. To the point it becomes impossible from frequencies higher than 100 Hz. This constraint on bandwidth can be used as well to design classical SISO systems.

It is important to highlight that the conclusions previously drawn are in accordance with rules of thumb adopted when the plant is treated as SISO. However, the previous mathematical proof and formalization cannot be found in the literature.

IV. CONTROL STRATEGY

A. Low-frequency controller

The frequency-dependent RGA analysis point out that the variables to directly controlled in low frequencies are $\tilde{i}_{1,q}$, $\tilde{i}_{2,q}$, $\tilde{i}_{2,d}$ and $\tilde{v}_{dc}$. The control of $\tilde{v}_{dc}$ indirectly controls the average active power drawn from the System 1, and, consequently $\tilde{i}_{1,d}$. To ensure null steady-state errors tracking achieve asymptotic reference tracking an integral action for each controlled variable must be included as following

$$\dot{\boldsymbol{x}}_i = \boldsymbol{\mathcal{A}}_i \boldsymbol{x}_i + \boldsymbol{\mathcal{B}}_i \boldsymbol{e}_i, \tag{4}$$

where $\boldsymbol{\mathcal{A}}_i = [\mathbf{0}_{4\times4}]$, $\boldsymbol{\mathcal{B}}_i = [\mathbf{I}_{4\times4}]$, $\boldsymbol{x}_i = [\, x_{q_1} \quad x_{d_2} \quad x_{q_2} \quad x_{dc}\,]^\intercal$ is the additional state, $\boldsymbol{e}_i = [\, e_{q_1} \quad e_{d_2} \quad e_{q_2} \quad e_{dc}\,]^\intercal$ is the error vector.

B. High-frequency controller

Unfortunately, in practice, undesirable harmonic components are generated compromising the power quality [23, 24, 25]. As a consequence, resonant modes must be included to mitigate these undesirable disturbances in the following manner

$$\dot{\boldsymbol{x}}_{j,k} = \boldsymbol{\mathcal{A}}_h \boldsymbol{x}_{j,k} + \boldsymbol{\mathcal{B}}_h e_{j,k}. \tag{5}$$

where $j \in \{1,2\}$ the subsystem side, $k \in \{d,q\}$, $\boldsymbol{x}_{j,k}$ $\mathbb{R}^2$ is the state vector, $e_{j,k}$ is the error, h is the harmonic order and

$$\boldsymbol{\mathcal{A}}_h = \begin{bmatrix} 0 & 1 \\ -(h\omega_j)^2 & -2\omega_c \end{bmatrix} \text{ and } \boldsymbol{\mathcal{B}}_h = \begin{bmatrix} 0 \\ 2\omega_c \end{bmatrix}, \tag{6}$$

where ω_c is resonant controller's bandwidth.

It should be highlighted that, according to Fig. 2, there is no constraint to control $\tilde{i}_{1,d}$, $\tilde{i}_{1,q}$ $\tilde{i}_{2,d}$ and $\tilde{i}_{2,q}$ for frequencies higher than 100 Hz. As shown in [25], the main unwanted components that distorts the ac-side currents are the negative sequence 5th and positive sequence 7th harmonics. Since the control law is implemented in the dq-frame, a single resonant controller for each axis is capable of compensating these harmonics at the same time [26]. Moreover, the resonance frequency must be tuned to $6\omega_1$ or 360 Hz. This frequency is higher than 100 Hz and, therefore it can be controlled regardless of the low frequency regulation.

C. Augmented system

Adding the aforementioned dynamics yields following open-loop system

$$\dot{\boldsymbol{x}}_a = \boldsymbol{\mathcal{A}}_a \boldsymbol{x}_a + \boldsymbol{\mathcal{B}}_a \boldsymbol{u} + \boldsymbol{\mathcal{B}}_{w_a} \boldsymbol{w} + \boldsymbol{\mathcal{B}}^* \boldsymbol{r}, \tag{7}$$

where

$$\boldsymbol{x}_a = \begin{bmatrix} \boldsymbol{x}^\intercal & \boldsymbol{x}_i^\intercal & \boldsymbol{x}_r^\intercal \end{bmatrix}^\intercal, \boldsymbol{r} = \begin{bmatrix} \boldsymbol{r}_i^\intercal & \boldsymbol{r}_r^\intercal \end{bmatrix}^\intercal,$$

$$\boldsymbol{\mathcal{A}}_a = \begin{bmatrix} \boldsymbol{\mathcal{A}} & \mathbf{0}_{5\times4} & \mathbf{0}_{5\times8} \\ -\boldsymbol{\mathcal{B}}_i \boldsymbol{\mathcal{C}}_i & \boldsymbol{\mathcal{A}}_i & \mathbf{0}_{4\times8} \\ -\boldsymbol{\mathcal{B}}_r \boldsymbol{\mathcal{C}}_r & \mathbf{0}_{8\times4} & \boldsymbol{\mathcal{A}}_r \end{bmatrix}, \boldsymbol{\mathcal{B}}_a = \begin{bmatrix} \boldsymbol{\mathcal{B}} \\ \mathbf{0}_{4\times4} \\ \mathbf{0}_{8\times4} \end{bmatrix}, \boldsymbol{\mathcal{B}}_{w_a} = \begin{bmatrix} \boldsymbol{\mathcal{B}}_w \\ \mathbf{0}_{4\times4} \\ \mathbf{0}_{8\times4} \end{bmatrix},$$

$$\boldsymbol{\mathcal{B}}^* = \begin{bmatrix} \mathbf{0}_{5\times4} & \mathbf{0}_{5\times4} \\ \boldsymbol{\mathcal{B}}_i & \mathbf{0}_{4\times4} \\ \mathbf{0}_{2\times4} & \mathbf{0}_{2\times4} \\ [\boldsymbol{\mathcal{B}}_6 \quad \mathbf{0}_{2\times3}] & \mathbf{0}_{2\times4} \\ [\mathbf{0}_{2\times1} \quad \boldsymbol{\mathcal{B}}_6 \quad \mathbf{0}_{2\times2}] & \mathbf{0}_{2\times4} \\ [\mathbf{0}_{2\times2} \quad \boldsymbol{\mathcal{B}}_6 \quad \mathbf{0}_{2\times1}] & \mathbf{0}_{2\times4} \end{bmatrix}. \tag{8}$$

$\boldsymbol{x}_r \in \mathbb{R}^8$ are the additional state variables regarding the resonant modes, and

$$\boldsymbol{\mathcal{A}}_r = \begin{bmatrix} \boldsymbol{\mathcal{A}}_6 & & & \\ & \boldsymbol{\mathcal{A}}_6 & & \\ & & \boldsymbol{\mathcal{A}}_6 & \\ & & & \boldsymbol{\mathcal{A}}_6 \end{bmatrix}, \boldsymbol{\mathcal{B}}_r = \begin{bmatrix} \boldsymbol{\mathcal{B}}_6 & & & \\ & \boldsymbol{\mathcal{B}}_6 & & \\ & & \boldsymbol{\mathcal{B}}_6 & \\ & & & \boldsymbol{\mathcal{B}}_6 \end{bmatrix}. \tag{9}$$

Additionally, $\boldsymbol{r}_i$ and $\boldsymbol{r}_r = \mathbf{0}$ are low- and high-frequency reference vectors, respectively.

V. Control law

The following control law

$$\boldsymbol{u} = -\boldsymbol{\mathcal{K}}\boldsymbol{x}_a, \tag{10}$$

where $\boldsymbol{\mathcal{K}} \in \mathbb{R}^{4\times 17}$ is used to achieve the desired performance and robustness.

To optimize the feedback matrix the infinity horizon linear-quadratic regulator (LQR) is applied. The LQR minimizes the following cost function

$$J = \frac{1}{2}\int_0^\infty (\boldsymbol{x}_a^\intercal(t)\mathbf{Q}\boldsymbol{x}_a(t) + \boldsymbol{u}^\intercal(t)\boldsymbol{\rho}\boldsymbol{u}(t))\, dt, \tag{11}$$

where $\mathbf{Q} \geq \mathbf{0} \in \mathbb{R}^{17\times 17}$ and $\boldsymbol{\rho} > \mathbf{0} \in \mathbb{R}^{4\times 4}$ [27, 28].

The main difficult during tuning controllers via LQR is to choose the matrices $\mathbf{Q}$ and $\boldsymbol{\rho}$. Therefore, it is proposed to use the following sensitivity function to aid in the processes.

$$\boldsymbol{\mathcal{S}}(s) = \frac{\boldsymbol{e}(s)}{\boldsymbol{r}(s)} = -\boldsymbol{\mathcal{C}}_a(s\mathbf{I} - (\boldsymbol{\mathcal{A}}_a - \boldsymbol{\mathcal{B}}_a\boldsymbol{\mathcal{K}}))^{-1}\boldsymbol{\mathcal{B}}^* + \mathbf{I}, \tag{12}$$

$$\boldsymbol{\mathcal{T}}(s) = \frac{\boldsymbol{y}(s)}{\boldsymbol{r}(s)} = \boldsymbol{\mathcal{C}}_a(s\mathbf{I} - (\boldsymbol{\mathcal{A}}_a - \boldsymbol{\mathcal{B}}_a\boldsymbol{\mathcal{K}}))^{-1}\boldsymbol{\mathcal{B}}^*. \tag{13}$$

It is important to highlight at this point that there are other design techniques that can be applied to find $\boldsymbol{\mathcal{K}}$. For instance, to ensure robustness against uncertainties in the model as well as in the grid, a robust design based on linear matrix inequalities (LMIs) can be used [29]. Nevertheless, regardless the chosen control design technique, the previous developed MIMO modeling and analysis is crucial.

A. Control law tuning

The MIMO bandwidth is defined as the frequency range between a lower frequency $\underline{\omega}_{bw}$ where the maximum singular value $\bar{\sigma}(\boldsymbol{\mathcal{T}}(j\omega))$ reaches $1/\sqrt{2}$, and a higher frequency $\bar{\omega}_{bw}$ where minimum singular value $\underline{\sigma}(\boldsymbol{\mathcal{T}}(j\omega))$ reaches $1/\sqrt{2}$. Additionally, minimizing $\|\boldsymbol{\mathcal{T}}(j\omega)\|_\infty$ and $\|\boldsymbol{\mathcal{S}}(j\omega)\|_\infty$ results in better transient response and robustness, respectively [17].

B. Plant's state variables ($q_{1,1}\ldots q_{5,5}$) choice

A procedure to ensure a systematic design can be achieved by keeping $\mathbf{Q}$ and ρ diagonal and choosing their weights apart. To do so ρ is primarily fixed as identity matrix. Furthermore, $\mathbf{Q}$ can also be subdivided into weights related to the plant's, integral and resonant state variable.

Initially, the plant's states ($q_{1,1}\ \ldots q_{5,5}$) are further subdivided into the fast dynamics ($\tilde{i}_{1,d}$, $\tilde{i}_{1,q}$, $\tilde{i}_{2,d}$, $\tilde{i}_{2,q}$) slow dynamics ($\tilde{v}_{dc}$) variables.

The maximum and minimum singular values os the sensitivity functions are depicted in Fig. 3 (a) and (b) for variations on the output currents' weights. For systematicity sake the previous values are kept equal and are varied in powers of then. The remaining values are $q_{i,i} = 1\ \forall i \in \{5, 6, \ldots, 16, 17\}$ and $\boldsymbol{\rho} = \mathbf{I}_4$. It should be highlighted that, according to Fig. 3, reducing the weights significantly increases $\bar{\omega}_{bw}$ value. As a result, the current reference signal tracking time reduces. Conversely, the speed comes with the cost of robustness as the value of $\|\boldsymbol{\mathcal{S}}(j\omega)\|_\infty$ increases. Therefore, a trade-off between these conflicting characteristic must be sought. Adopting $q_{1,1}\ldots q_{4,4} = 10^{-8}$ good trade-off is found.

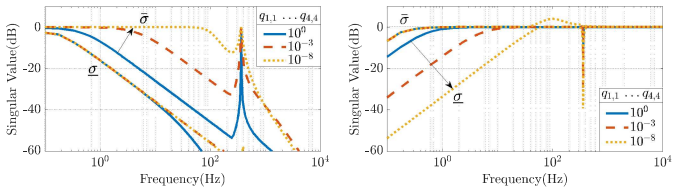

(a) $\bar{\sigma}(\boldsymbol{\mathcal{T}}(j\omega))$ and $\underline{\sigma}(\boldsymbol{\mathcal{T}}(j\omega))$. (b) $\bar{\sigma}(\boldsymbol{\mathcal{S}}(j\omega))$ and $\underline{\sigma}(\boldsymbol{\mathcal{S}}(j\omega))$.

Fig. 3. Frequency response under variations of $q_{1,1}\ldots q_{4,4}$ with $q_{i,i} = 1\ \forall i \in \{5, 6, \ldots, 16, 17\}$ and $\boldsymbol{\rho} = \mathbf{I}_4$.

Besides, the previous variations have almost no effect $\underline{\omega}_{bw}$. This is due the fact that the lower bandwidth frequency is tied to the slow dynamics of $\tilde{v}_{dc}$. Consequently, to ensure fast regulation of $\tilde{v}_{dc}$ its respective weight $q_{5,5}$ is reduced, as depicted in Fig. 4. This reduction presents virtually no effect in $\bar{\sigma}(\boldsymbol{\mathcal{T}}(j\omega))$ and $\underline{\sigma}(\boldsymbol{\mathcal{S}}(j\omega))$. Conversely, there is a increase in $\underline{\sigma}(\boldsymbol{\mathcal{T}}(j\omega))$. A suitable choice is found to be $q_{5,5} = 10^{-5}$.

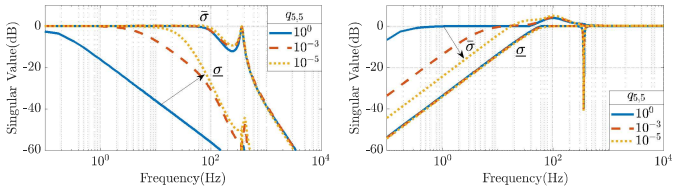

(a) $\bar{\sigma}(\boldsymbol{\mathcal{T}}(j\omega))$ and $\underline{\sigma}(\boldsymbol{\mathcal{T}}(j\omega))$. (b) $\bar{\sigma}(\boldsymbol{\mathcal{S}}(j\omega))$ and $\underline{\sigma}(\boldsymbol{\mathcal{S}}(j\omega))$.

Fig. 4. Frequency response under variation of $q_{5,5}$ with $q_{1,1}\ldots q_{4,4} = 10^{-8}$, $q_{i,i} = 1\ \forall i \in \{6, \ldots, 16, 17\}$ and $\boldsymbol{\rho} = \mathbf{I}_4$.

C. Integral state variables weights ($q_{6,6}\ \ldots q_{9,9}$) selection

Increasing the integral state variables weights increase the maximum and minimum singular values together of the sensitivity functions as shown in Fig. 5. As a consequence, there is no effect on bandwidth. Additionally $\|\boldsymbol{\mathcal{S}}(j\omega)\|_\infty$ reduces, increasing the systems robustness.

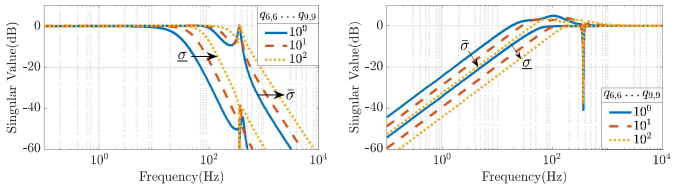

(a) $\bar{\sigma}(\boldsymbol{\mathcal{T}}(j\omega))$ and $\underline{\sigma}(\boldsymbol{\mathcal{T}}(j\omega))$. (b) $\bar{\sigma}(\boldsymbol{\mathcal{S}}(j\omega))$ and $\underline{\sigma}(\boldsymbol{\mathcal{S}}(j\omega))$.

Fig. 5. Frequency response under variation of $q_{6,6}\ldots q_{9,9}$ with $q_{1,1}\ldots q_{4,4} = 10^{-8}$, $q_{5,5} = 10^{-5}$, $q_{i,i} = 1\ \forall i \in \{10, \ldots, 16, 17\}$ and $\boldsymbol{\rho} = \mathbf{I}_4$.

Notice that changing the values of $q_{6,6}$, $q_{7,7}$, $q_{8,8}$ and $q_{9,9}$ has a direct impact on $\tilde{i}_{1,q}$, $\tilde{i}_{2,d}$, $\tilde{i}_{2,q}$ and $\tilde{v}_{dc}$ dynamics, respectively. Based on the previous analysis it was chosen $q_{7,7} = 10$, $q_{6,6} = q_{8,8} = 5\times 10^3$ and $q_{9,9} = 10^{-3}$. Consequently, $\tilde{i}_{1,q}$, $\tilde{i}_{2,q}$ present the shortest transient, while $\tilde{v}_{dc}$ the longest settling time. It is important to highlighted

that the d- and q-axis currents weights are purposely chosen to be different. This was done to show that their dynamics does not need to be the same, as well as to show the distinct time constants in the experimental results.

D. Resonant modes weighting tune ($q_{10,10} \dots q_{17,17}$)

To achieve a fast disturbance rejection, the resonance bandwidth must be widened. This can be achieved by increasing the weights related to the respective resonant state variables as depicted in Fig. 6 (b). Also notice that $\underline{\omega}_{bw}$ and $\bar{\omega}_{bw}$ have not changed.

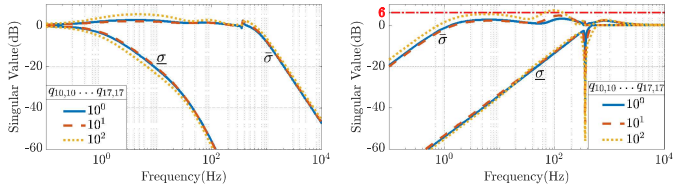

(a) $\bar{\sigma}(\boldsymbol{\mathcal{T}}(j\omega))$ and $\underline{\sigma}(\boldsymbol{\mathcal{T}}(j\omega))$. (b) $\bar{\sigma}(\boldsymbol{\mathcal{S}}(j\omega))$ and $\underline{\sigma}(\boldsymbol{\mathcal{S}}(j\omega))$.

Fig. 6. Frequency response under variation of $q_{10,10} \dots q_{17,17}$ with $q_{1,1} \dots q_{4,4} = 10^{-8}$, $q_{5,5} = 10^{-5}$, $q_{7,7} = 10$, $q_{6,6} = q_{8,8} = 5 \times 10^3$, $q_{9,9} = 10^{-3}$ and $\boldsymbol{\rho} = \mathbf{I}_4$.

It should be highlighted that high values of weights, even though make the time response faster, may result in poor transitory response as the infinity norm value increases. This fact can be seen in Fig. 6 (a) that for 10^2 the peak of $\bar{\sigma}(\boldsymbol{\mathcal{T}}(j\omega))$ is 1.82. Moreover, increasing the weights also increases the infinite norm of the sensitivity matrix, to the point of reducing the robustness level to unacceptable values (higher than 6 dB). Therefore, to reduce $\|\boldsymbol{\mathcal{S}}(j\omega)\|_\infty$ and $\|\boldsymbol{\mathcal{T}}(j\omega)\|_\infty$ to recommended levels, according to [17], keeping them at 1.42 and 1.33, respectively, it was chosen the resonant weights equal to 3×10^{-3}. Moreover, it has chosen $\omega_c = 20\,\mathrm{rad/s}$.

E. Control variable weighting (ρ)

The control effort can be minimized by choosing relatively large ρ. This, in turn, makes the whole system slower, as depicted in Fig. 7. But, on the good side, increases the robustness by reducing $\|\boldsymbol{\mathcal{S}}(j\omega)\|_\infty$. Consequently, a trade-off was found choosing $\boldsymbol{\rho} = 10^{-1} \times \mathbf{I}_4$, resulting in $\|\boldsymbol{\mathcal{T}}(j\omega)\|_\infty = 1.09$, $\|\boldsymbol{\mathcal{S}}(j\omega)\|_\infty = 1.33$, $\bar{\omega}_{bw} = 1.2\,\mathrm{kHz}$ and $\underline{\omega}_{bw} = 3.5\,\mathrm{Hz}$.

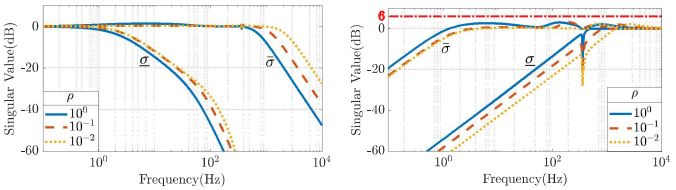

(a) $\bar{\sigma}(\boldsymbol{\mathcal{T}}(j\omega))$ and $\underline{\sigma}(\boldsymbol{\mathcal{T}}(j\omega))$. (b) $\bar{\sigma}(\boldsymbol{\mathcal{S}}(j\omega))$ and $\underline{\sigma}(\boldsymbol{\mathcal{S}}(j\omega))$.

Fig. 7. Frequency response under variation of $\boldsymbol{\rho} = \rho\mathbf{I}_4$ $q_{10,10} \dots q_{17,17}$ with $q_{1,1} \dots q_{4,4} = 10^{-8}$, $q_{5,5} = 10^{-5}$, $q_{7,7} = 10$, $q_{6,6} = q_{8,8} = 5 \times 10^3$, $q_{9,9} = 10^{-3}$ and $q_{10,10} = \dots = q_{17,17} = 3 \times 10^{-3}$.

VI. EXPERIMENTAL EVALUATION

A prototype, shown in Figure 8, is used to test the proposed control law. It comprises: (1,10) protection fuses; (2,3,11) command devices circuitry; (4) auxiliary resistors; (5) auxiliary sources; (6,7,8) conditioning circuitry; (9,13) voltage and current sensors; (12) output filters (capacitors are bypassed); (14) BTB converter; (15) driving semiconductor switches circuitry. The prototype parameters are given in

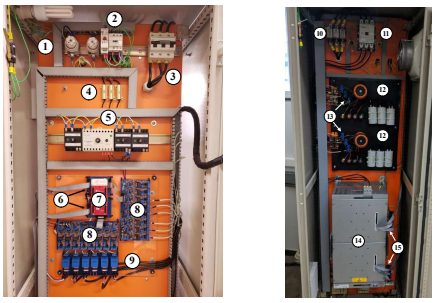

(a) Conditioning side. (b) Power side.

Fig. 8. Experimental setup.

Table I.

A transformer with a ratio of 2:1 is used on the ac-side of System 2 to ensure isolation between the two ac-sides, since they are powered by the same electrical network. As a consequence, the nominal peak voltage of System 2 is 90 V.

Fig. 9 (a) shows the dc-side voltage and phase b current waveforms of System 1 and 2, in steady-state. The references values are $i^*_{2,d} = -13\,\mathrm{A}$, $i^*_{1,q} = i_{2,q} = 0\,\mathrm{A}$ and $v^*_{dc} = 400\,\mathrm{V}$. Therefore, the rms value of $i_{2,b}$ should be around $13/\sqrt{2} \approx 9.2\,\mathrm{A}$. Furthermore, to keep the active power balance between sides and, taking into consideration that the voltage level at side 1 is half of side 2, $i_{1,b} \approx 4.6\,\mathrm{A}$ (rms) for a lossless converter. However, for the real converter $i_{1,b} \approx 5.87\,\mathrm{A}$ (rms) to account for the losses. Consequently, although $i_{1,d}$ is not directly controlled, it settles in the correct value in order to regulate the dc-side voltage at its reference.

The voltage and current at both sides, under the same operating condition, are depicted in Fig. 9 (b). Notice that, according to the notation adopted in Fig. 1, $i_{2,b}$ lags 180° in relation to $v_{g_{2,b}}$ since its reference is negative and $i_{1,b}$ is in phase with $v_{g_{1,b}}$. This ensures the correct active power balance between the sides.

Fig. 10 (a) and (b) show the phase b currents waveforms of System 1 and 2 for reactive power synthesis on both sides. The references are $i^*_{1,q} = -8\,\mathrm{A}$ and $i^*_{2,q} = 8\,\mathrm{A}$, respectively. While, $i^*_{2,d} = 0\,\mathrm{A}$, and $v^*_{dc} = 400\,\mathrm{V}$. It can be clearly seen that in the first case (Fig. 10 (a)) that the current $i_{1,b}$ is delayed by approximately 90° in relation to $v_{g_{1,b}}$. On the other hand, $i_{2,b}$ is ahead of the voltage $v_{g_{2,b}}$ by around 90°. It should be highlighted that in both cases, to keep the dc-side voltage regulated, there will be a value of $i_{1,d}$ that is different from zero to account for the losses.

In order to evaluate the transient behavior of the system it was tested under active and reactive power steps. Fig. 11 (a) shows the waveform of both ac-side and dc-voltage during

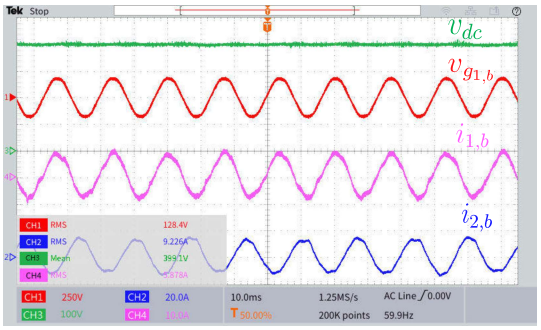

(a) dc-side voltage (v_{dc}); System 1 ac-side voltage ($v_{g_{1,b}}$); System 1 ac-side current ($i_{1,b}$); System 2 ac-side current ($i_{2,b}$).

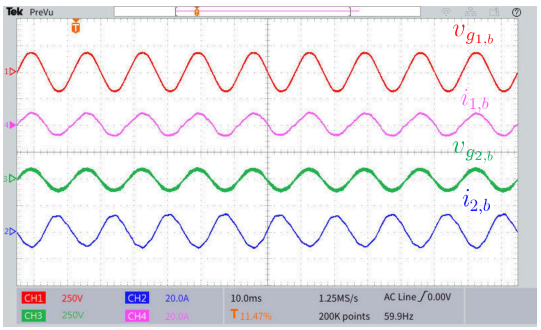

(b) System 1 ac-side voltage ($v_{g_{1,b}}$); System 1 ac-side current ($i_{1,b}$); System 2 ac-side voltage ($v_{g_{2,b}}$); System 2 ac-side current ($i_{2,b}$).

Fig. 9. Waveforms for active power management.

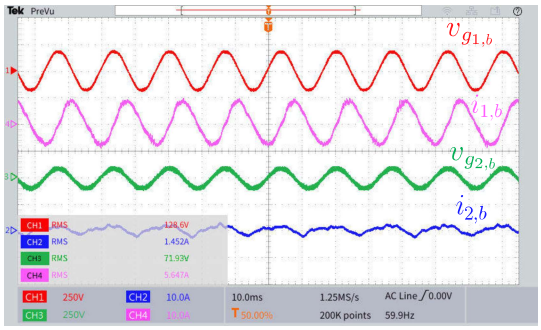

(a) System 1 ac-side voltage ($v_{g_{1,b}}$); System 1 ac-side current ($i_{1,b}$); System 2 ac-side voltage ($v_{g_{2,b}}$); System 2 ac-side current ($i_{2,b}$).

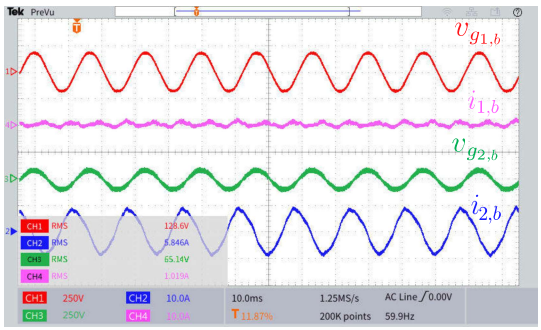

(b) System 1 ac-side voltage ($v_{g_{1,b}}$); System 1 ac-side current ($i_{1,b}$); System 2 ac-side voltage ($v_{g_{2,b}}$); System 2 ac-side current ($i_{2,b}$).

Fig. 10. Waveforms for reactive power management.

active power step. In the 'a' event, the System 2 active power reference is changed from 0 to $-2.7\,\mathrm{kW}$, while in 'b' it is changed back to $0\,\mathrm{kW}$. It can be clearly seen that the current response for both sides is fast and smooth, without overshot. Moreover, the dc-side voltage control responds relatively fast with an overshoot less than 10%. Additionally, the settling times are in accordance with the designed bandwidth region $\bar{\omega}_{bw} = 1.2\,\mathrm{kHz}$ and $\underline{\omega}_{bw} = 3.5\,\mathrm{Hz}$, being the v_{dc} dynamics the slowest one.

Fig. 11 (b) depicts the system response under reactive power steps. Between the events 'c' and 'd' there is a variation from 0 to $1.35\,\mathrm{kvar}$ and back to $0\,\mathrm{kvar}$ in System 1. While between events 'e' and 'f' the reactive power at System 2 is changed from 0 to $2.7\,\mathrm{kvar}$ and back to $0\,\mathrm{kvar}$. Notice that the system quickly tracks the reference without any overshoot. Moreover, it is clear that this time constant is smaller than the $i_{2,d}$ one, which is in accordance with the design. It should be also highlighted that when the System 2 is synthesizing reactive power there will be a consumption of active power from System 1, side where the active power is not directly regulated, to account for the losses. That is the reason why there is a small variation in the dc-side voltage. This phenomenon can be seen in Fig. 11 (b).

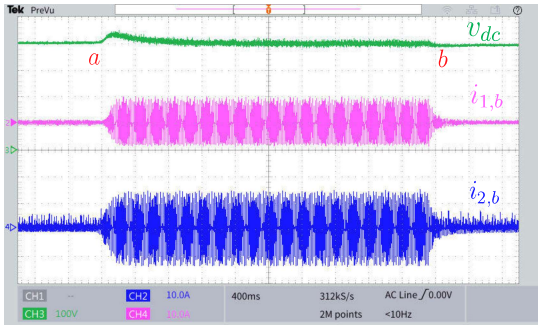

(a) Transient response for active power steps.

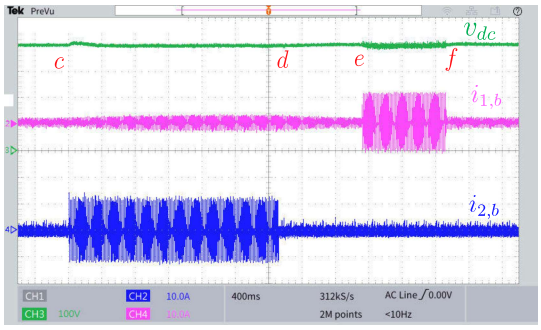

(b) Transient response for reactive power steps.

Fig. 11. System behavior under active an reactive power step changes.

VII. CONCLUSION

This work presented the analysis and proposed a control law and its design through the lens of multiple-input multiple-output systems. The suitable choice of the directly controlled variables a function of the frequency was performed based on the frequency-dependent relative gain

array results. Physical interpretation supports the mathematical theoretical analysis. Additionally, the conclusion drawn are in with rules of thumbs used when the plant is treated as single-input single-ouput. However, in the paper the mathematical proof and formalization are comprehensively detailed. The frequency-dependent relative gain array was used to choose the suitable low- and high-frequency controllers. Sensitivity functions were used to tune linear quadratic regulator. Experimental results have validated the analysis and demonstrated the effectiveness of the proposed technique.

REFERENCES

[1] T. Friedli, J. W. Kolar, J. Rodriguez, and P. W. Wheeler, "Comparative evaluation of three-phase AC–AC matrix converter and voltage DC-link back-to-back converter systems," *IEEE Transactions on Industrial Electronics*, vol. 59, no. 12, pp. 4487–4510, Dec. 2012.

[2] A. Rodriguez-Cabero, M. Prodanovic, and J. Roldan-Perez, "Full-state feedback control of back-to-back converters based on differential and common power concepts," *IEEE Transactions on Industrial Electronics*, vol. 66, no. 11, pp. 9045–9055, Nov. 2019.

[3] L. Shen, S. Bozhko, C. I. Hill, and P. Wheeler, "DC-link capacitor second carrier band switching harmonic current reduction in two-level back-to-back converters," *IEEE Transactions on Power Electronics*, vol. 33, no. 4, pp. 3567–3574, Apr. 2018.

[4] J. Alcala, V. Cardenas, A. R. Ramirez-Lopez, and J. Gudino-Lau, "Study of the bidirectional power flow in back-to-back converters by using linear and nonlinear control strategies," in *2011 IEEE Energy Conversion Congress and Exposition*. IEEE, Sep. 2011.

[5] C.-Y. Tang, Y.-F. Chen, Y.-M. Chen, and Y.-R. Chang, "DC-link voltage control strategy for three-phase back-to-back active power conditioners," *IEEE Transactions on Industrial Electronics*, vol. 62, no. 10, pp. 6306–6316, Oct. 2015.

[6] A. Yazdani and R. Iravani, *Voltage-Sourced Converters in Power Systems Modeling, Control, and Applications*. Wiley & Sons, Incorporated, John, 2010.

[7] P. Albertos and S. Antonio, *Multivariable Control Systems An Engineering Approach*. Springer London, Limited, 2006.

[8] D. Jovcic, L. Lamont, and K. Abbott, "Control system design for VSC transmission," *Electric Power Systems Research*, vol. 77, no. 7, pp. 721–729, May 2007.

[9] S. A. Khajehoddin, M. Karimi-Ghartemani, and M. Ebrahimi, "Optimal and systematic design of current controller for grid-connected inverters," *IEEE Journal of Emerging and Selected Topics in Power Electronics*, vol. 6, no. 2, pp. 812–824, Jun. 2018.

[10] P. M. de Almeida, A. S. B. Ribeiro, I. D. N. Souza, M. de C. Fernandes, G. A. Fogli, V. Cuk, P. G. Barbosa, and P. F. Ribeiro, "Systematic design of a DLQR applied to grid-forming converters," *IEEE Journal of Emerging and Selected Topics in Industrial Electronics*, vol. 1, no. 2, pp. 200–210, Oct. 2020.

[11] A. Tabesh and R. Iravani, "Multivariable dynamic model and robust control of a voltage-source converter for power system applications," *IEEE Transactions on Power Delivery*, vol. 24, no. 1, pp. 462–471, Jan. 2009.

[12] B. Bahrani, M. Saeedifard, A. Karimi, and A. Rufer, "A multivariable design methodology for voltage control of a single-DG-unit microgrid," *IEEE Transactions on Industrial Informatics*, vol. 9, no. 2, pp. 589–599, May 2013.

[13] M. Karimi-Ghartemani and H. Karimi, "A robust multivariable approach for current control of voltage-source converters in synchronous frame," *IEEE Journal of Emerging and Selected Topics in Power Electronics*, vol. 9, no. 5, pp. 6174–6183, Oct. 2021.

[14] M. Ochoa-Giménez, A. García-Cerrada, and J. L. Zamora-Macho, "Comprehensive control for unified power quality conditioners," *Journal of Modern Power Systems and Clean Energy*, vol. 5, no. 4, pp. 609–619, Jul. 2017.

[15] A. Rodriguez-Cabero, F. H. Sanchez, and M. Prodanovic, "A unified control of back-to-back converter," in *2016 IEEE Energy Conversion Congress and Exposition (ECCE)*. IEEE, Sep. 2016.

[16] P. Rodriguez, R. Teodorescu, I. Candela, A. Timbus, M. Liserre, and F. Blaabjerg, "New positive-sequence voltage detector for grid synchronization of power converters under faulty grid conditions," in *37th IEEE Power Electronics Specialists Conference*. IEEE, 2016.

[17] S. Skogestad and I. Postlethwaite, *Multivariable Feedback Control Analysis and Design*. Wiley & Sons, Limited, John, 2005.

[18] I. D. N. Souza, P. M. de Almeida, G. A. Fogli, P. G. Barbosa, and P. F. Ribeiro, "Multivariable optimal control applied to a back-to-back power converter," *IEEE Transactions on Industrial Electronics*, vol. 69, no. 9, pp. 9406–9418, Sep. 2022.

[19] M. Hovd and S. Skogestad, "Simple frequency-dependent tools for control system analysis, structure selection and design," *Automatica*, vol. 28, no. 5, pp. 989–996, Sep. 1992.

[20] J.-W. Chang and C.-C. Yu, "The relative gain for non-square multivariable systems," *Chemical Engineering Science*, vol. 45, no. 5, pp. 1309–1323, 1990.

[21] K. Harve and S. Skogestad, "Input/output selection and partial control," *IFAC Proceedings Volumes*, vol. 29, no. 1, pp. 5977–5982, Jun. 1996.

[22] Y. Cao, "Control structure selection for chemical processes using input-output controllability analysis," Ph.D. dissertation, University of Exeter, 1995.

[23] P. M. Almeida, P. G. Barbosa, J. G. Oliveira, J. L. Duarte, and P. F. Ribeiro, "Digital proportional multi-resonant current controller for improving grid-connected photovoltaic systems," *Renewable Energy*, vol. 76, pp. 662–669, Apr. 2015.

[24] P. M. Almeida, J. L. Duarte, P. F. Ribeiro, and P. G. Barbosa, "Repetitive controller for improving grid-connected photovoltaic systems," *IET Power*

Electronics, vol. 7, no. 6, pp. 1466–1474, Jun. 2014.

[25] G. A. Fogli, R. L. Valle, P. M. de Almeida, and P. G. Barbosa, "A simple dead-time compensation strategy for grid-connected voltage-sourced converters semiconductor switches," *Electric Power Systems Research*, vol. 174, p. 105853, Sep. 2019.

[26] M. Liserre, R. Teodorescu, and F. Blaabjerg, "Multiple harmonics control for three-phase grid converter systems with the use of PI-RES current controller in a rotating frame," *IEEE Transactions on Power Electronics*, vol. 21, no. 3, pp. 836–841, May 2006.

[27] B. D. O. Anderson and J. B. Moore, *Optimal Control*. Dover Publications, 2007.

[28] E. Ostertag, *Mono- and Multivariable Control and Estimation*. Springer-Verlag Berlin Heidelberg, 2011.

[29] C. R. D. Osorio, G. G. Koch, H. Pinheiro, R. C. L. F. Oliveira, and V. F. Montagner, "Robust current control of grid-tied inverters affected by LCL filter soft-saturation," *IEEE Transactions on Industrial Electronics*, vol. 67, no. 8, pp. 6550–6561, Aug. 2020.